

Structural Insights Into Amyloid Polymorphism: The Impact of Glutamine to Norleucine Substitutions in GNNQQNY Aggregation

Fruzsina Bencs,^[a, b] Loránd Románszki,^[c] Viktor Farkas,^[d] and András Perczel^{*,[a, d]}

Polypeptides can self-assemble into highly organized amyloid structures through complex and poorly understood mechanisms. To better understand the key parameters governing amyloidogenesis, we investigated the aggregation of the Sup35 prion-derived GNNQQNY sequence alongside two rationally designed mutants, glutamine to norleucine in the 4th or 5th position, where selective removal of hydrogen bonding capacity reduces amyloid structural stability. Our findings reveal that **β -sheet arrays** form rapidly as an initial step, followed by π – π aromatic interactions between Tyr residues, which drive hierarchical self-assembly into 3D fibrillar structures via hydrophobic zippers and partial water exclusion. As the oligomers grow, they also acquire twist and chirality at the protofilament level, with

Tyr ladders serving as key interaction surfaces that dictate the final amyloid architecture. These ladders guide protofibrils to assemble into either oppositely twisted chiral fibers or achiral nanocrystals, contributing to amyloid polymorphism. The emergence of distinct polymorphs is influenced by multiple factors, including fibril twisting, side-chain interactions, solvent exclusion, and local microenvironmental conditions. Our study provides crucial insights into the hierarchical nature of amyloid self-assembly and highlights the structural adaptability of amyloid fibrils, which is essential for designing functional amyloids and understanding the pathogenicity of disease-associated aggregates.

1. Introduction

Proteins that lose their native structure can either be refolded by chaperones, degraded, or self-assemble into highly ordered

amyloid aggregates. Even partial unfolding can expose hidden structural features, leading to metastable states that drive amyloid formation. While cryo-EM has provided detailed 3D structures of mature amyloid fibrils,^[1] understanding early-stage self-assembly remains a critical challenge. Our goal was to track amyloid formation at every hierarchical stage, from unstructured monomers to highly complex nano- and meso-sized fibrils. We focused on GNNQQNY, a heptapeptide derived from the Sup35 yeast prion protein, which is an aggregation-prone region (APR).^[2–5] This sequence is a widely studied model due to its high intrinsic amyloidogenicity and well-defined steric zipper interactions. We examined the molecular events of β -sheet formation and explored how environmental conditions (pH, temperature) and sequence modifications influence amyloid assembly. Using chiroptical spectroscopy and microscopy, we monitored amyloid growth in real-time, while targeted point mutations allowed us to disrupt key stabilizing interactions and probe their role in fibril formation.

Amyloid self-assembly occurs through a multi-step process, beginning with primary nucleation, followed by elongation, secondary nucleation, and fragmentation, ultimately leading to sigmoidal growth curves.^[6] The primary nucleation phase—where monomers misfold and aggregate into a stable nucleus—dictates the course of fibril formation. This step is often the slowest and involves the alignment of β -strands into transient oligomers, which serve as reactive templates for further growth. These soluble oligomers, enriched in β -edges and β -layers, represent the most cytotoxic amyloid species, capable of disrupting cellular processes.^[7,8] As elongation proceeds, hydrophobic steric zippers reinforce amyloid stability, but solubility decreases, making this stage difficult to monitor. Ultimately, fibrils mature

[a] F. Bencs, A. Perczel

Laboratory of Structural Chemistry and Biology, Institute of Chemistry, ELTE Eötvös Loránd University, Pázmány Péter sétány 1/A, Budapest, Hungary
E-mail: perczel.andras@tk.elte.hu

[b] F. Bencs

ELTE Hevesy György PhD School of Chemistry, ELTE Eötvös Loránd University, Pázmány Péter sétány 1/A, Budapest, Hungary

[c] L. Románszki


HUN-REN Research Centre for Natural Sciences, Institute of Materials and Environmental Chemistry, Magyar tudósok körútja 2, Budapest, Hungary

[d] V. Farkas, A. Perczel

HUN-REN – ELTE Protein Modeling Research Group, ELTE Eötvös Loránd University, Pázmány Péter sétány 1/A, Budapest, Hungary

Abbreviations: -NH₂, amide protection of C-terminal; Ac, acetyl protection of N-terminal; AFM, atomic force microscopy; APR, aggregation-prone region; B-type spectrum, β -plated backbone; c, peptide concentration in [mmol/dm³] = mM; ECD, electronic circular dichroism; FTIR, Fourier transform infrared spectroscopy; FUV, far-ultraviolet range (185–260 nm); h_p, peak height; h_v, valley height; L_{pp}, peak-to-peak distance; MeCN, acetonitrile; Nle, norleucine; Sc, shape complementarity; TFA, trifluoroacetic acid; U-type spectrum, unstructured backbone; VCD, vibrational circular dichroism.

 Supporting information for this article is available on the WWW under <https://doi.org/10.1002/chem.202404255>

 © 2025 The Author(s). Chemistry – A European Journal published by Wiley-VCH GmbH. This is an open access article under the terms of the [Creative Commons Attribution-NonCommercial](https://creativecommons.org/licenses/by-nc/4.0/) License, which permits use, distribution and reproduction in any medium, provided the original work is properly cited and is not used for commercial purposes.

into micron- to nanoscale structures, whose architecture can be resolved by solid-state techniques like x-ray crystallography and electron microscopy.^[1,9] A defining feature of amyloids is polymorphism, arising from variations in: i) monomeric arrangement within the amyloid core, strongly influenced by sequence. ii) Protofibril interactions, leading to different fibril morphologies. iii) Twist periodicity, affecting fibril packing and stability. iv) Interface formation, modifying physicochemical properties like fragmentation rates and secondary nucleation efficiency. These findings apply regardless of the peptide sequence. Several examples can be found by examining polymorphisms of small peptides.^[10]

Molecular dynamics simulations have demonstrated that the aggregation of the GNNQQNY peptide exhibits significant structural polymorphism in its early stages and follows classical nucleation theory, with critical nucleus sizes of 4–5 monomers at 280 K and 5–6 monomers at 300 K.^[11] These simulations have also provided crucial insights into the molecular mechanisms governing amyloid fibril formation and the key factors influencing fibril stability.^[12–14] In addition, the combination of solid-state NMR and molecular dynamics simulations has offered a dynamic perspective on the aggregation process, shedding light on the kinetics of fibril formation and structural transitions.^[15,16] These findings collectively contribute to a deeper understanding of how peptide sequence and environmental conditions dictate amyloid polymorphism and stability.

The polymorphism of full-length amyloidogenic proteins can be effectively modeled using shorter APRs,^[17,18] making GNNQQNY an ideal system for dissecting these effects. For GNNQQNY amyloids, polymorphism primarily affects β -sheet pairing and the spatial arrangement of steric zippers and water channels.^[19,20] (Figure 1) Structural studies of two distinct polymorphs (PDB ID: 1YJP and 2OMM) reveal significant differences in their packing. While i) polymorph A exhibits a looser structure, stabilized by extensive Tyr stacking and hydration shells, ii) polymorph B is more tightly packed, forming narrow water channels with fewer inter-sheet aromatic interactions.

To investigate the role of side-chain interactions in these polymorphic transitions, we replaced Gln with norleucine (Nle), which mimics its spatial properties but lacks hydrogen bonding capacity. This strategic mutation enabled us to destabilize specific interactions and probe their contributions to amyloid stability and polymorphism. By targeting hydrogen bonding networks and steric zippers, we provide new mechanistic insights into amyloid architecture and its implications for biomaterial design and disease pathology.

2. Results and Discussion

2.1. How pH Affects Amyloid Formation of GNNQQNY?

The GNNQQNY oligopeptide can adopt a range of protonation states, creating a formal total charge range between +1.0 (with a protonated N-terminus) and –2.0 (with both the C-terminus and Y7 deprotonated) (Figure 2f). We systematically examined

the peptide's amyloidity across this range by recording electronic circular dichroism (ECD) spectra at different pH values: pH 2.4 ($\delta = +1.0$), pH 3.6 ($\delta = +0.5$), pH 5.5 ($\delta = 0$), pH 7.5 ($\delta = -0.5$), and pH 9.0 ($\delta = -1.0$), to assess the peptide's self-assembly over time ($0 \leq t \leq 40$ h) (Figure 2a–e). Measurements were conducted at 37°C with stirring to ensure reproducibility, and peptide concentrations were set between 0.5–0.6 mM to optimize the ECD time window. We observed that the U→B (unstructured to β -sheet) transition could not be detected at either strongly acidic (pH < 2.4) or basic (pH 9.0) conditions, even after 40 h of incubation, suggesting that unbalanced charges at the N- and C-termini inhibit β -strand formation (Figure 2a–e). At extreme pH values, electrostatic repulsion prevents chain ordering, favoring monomeric states. In contrast, at more neutral pH ranges ($2.5 < \text{pH} < 10.5$), partial charges on both the N- and C-termini facilitated ordering of the peptide chains, resulting in β -strand formation, although the required time varied (Figure 2c). The pH-controlled charge distribution affected the rate of amyloid formation by influencing the concentration of the supersaturated solution, with moderate pH values (between 2.5 and 10.5) allowing for an optimal arrangement of interchain interactions (Figure 2b,d). This pH range suggests that attractive forces between charged terminals lead to the formation of a common hydrate shell where the peptide chains gradually align and form H-bonds, overcoming the repulsive forces of like charges. These considerations highlight the importance of charge balance in amyloid-like self-assembly and the role of gatekeeper residues (e.g., D, E, K, R) in the process.^[22,23] Testing of single- and double-end protected derivatives confirmed that charge balance is a critical factor for initiating amyloid formation (Figure S3a).

2.2. Solubility and Structural Transitions of Protected GNNQQNY Heptapeptides

All four differently protected GNNQQNY heptapeptides (Figure S4) exhibit similar B-type ECD spectra, characterized by a negative maximum at ~190–195 nm and a positive maximum at ~200–205 nm, indicative of β -sheet secondary structure. Interestingly, the unprotected GNNQQNY sequence displays an additional negative band at ~220 nm, which corresponds to a distinct conformational feature. Gaussian decomposition of the spectra reveals that the component curves closely overlap, suggesting a similar molecular backbone across the different peptide variants (Figure S4b). Despite the common spectral features, the structural differences between the protected and unprotected peptides highlight the influence of terminal modifications on the overall peptide behavior.

APR motifs, such as GNNQQNY, typically require charged N- and/or C-terminals to maintain solubility, as they often contain hydrophobic residues. However, an APR with both termini protected is even less soluble. For example, the Ac-GNNQQNY-NH₂ variant remains insoluble in water until the phenolic hydroxyl group of Y7 is deprotonated, leading to a solubility transition around pH 10. Despite this solubility shift, the peptide immediately adopts a β -sheet amyloid structure as indicated by its ECD spectra, preventing detection of the initial unstructured

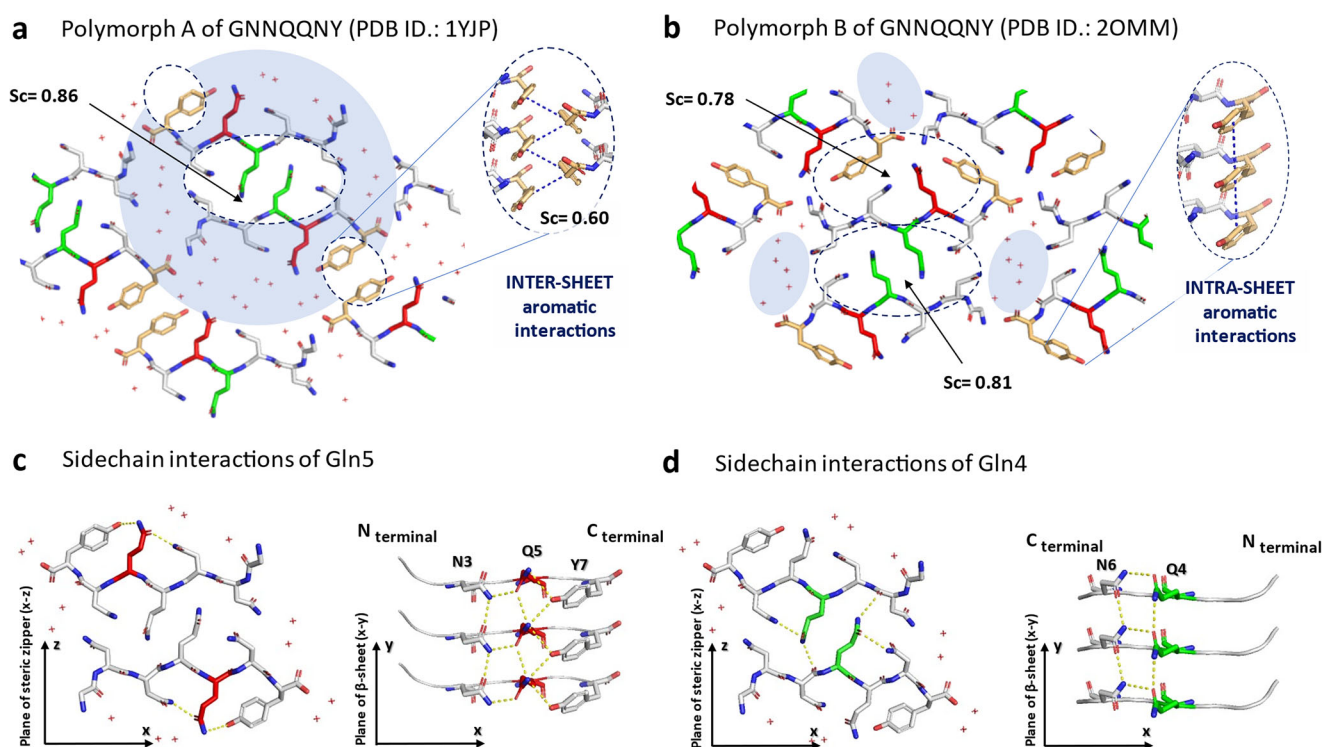


Figure 1. Crystal structure comparison of two GNNQQNY polymorphs (A-1YJP; B-2OMM). The steric zipper symmetry remains consistent between the two polymorphs; however, there are significant differences in the spatial organization of the amyloid fibrils generated by these zippers. **a**) In the case of 1YJP, a more looser packing structure develops with a hydrate shell surrounding the β -sheet pairs. Two interfaces are formed, one between the sheets (with a shape complementarity,^[21] $Sc = 0.86$) and the other between the Tyr-ladders ($Sc = 0.60$) resulting in a more extensive network of aromatic interactions. **b**) Conversely, 2OMM shows a tighter packing arrangement ($Sc = 0.78$ and $Sc = 0.81$) with water channels and only intra-sheet interactions between aromatic side chains. **c–d**) Interactions formed by interstrand Q5, Q4 side-chains. The crystal structures reveal the nature of the interactions that enhance the stability of the amyloid structure, such as the hydrogen bonds formed between the β -stranded backbones and the so-called Asn- and Gln-ladders, formed between their side-chains. The hydrogen bonds drawn in yellow dots stabilizes the 3D-structure of amyloids via Q4 and Q5 interstrand ladders. Glutamine in the 5th position can not only form an amide-ladder within the β -sheet, but also anchor the two adjacent side-chains (N3, Y7), which can provide a high degree of stability to the forming amyloid and contribute to the formation of the Tyr ladder (**c**, right). In contrast, glutamine in the 4th position can only anchor one side-chain but can form an interstrand amide-ladder and stabilize the steric zipper by forming inter-sheet hydrogen bonds (**d**, right).

monomeric form (Figure S3h). This behavior suggests that the structural transitions to β -sheet formation are closely linked to changes in solubility, emphasizing the impact of terminal modifications on amyloid formation.

2.3. Effect of Increasing Concentration on Amyloid Structure

To explore the effect of concentration on amyloid formation under acidic conditions with partially balanced charges ($+0.85 < \delta < +0.50$, $2.8 < \text{pH} < 3.6$), we varied the concentration range from 0.55 to 2.0 mM. The initial indication of oligomer formation is seen in the changes of ECD spectral shapes (Figure 3b), with the appearance of characteristic β -sheet signals: a negative maximum at ~ 188 nm, a positive one at ~ 205 nm, and another negative maximum at ~ 225 nm. This transformation progresses through a time-consuming process from oligomeric β -strands to β -sheets, protofibrils, and finally mature fibrils, with increasing molecular complexity.

While the initial shift from disordered to β -backbone structure causes a significant U \rightarrow B ECD spectral shift, further amyloid assembly only causes minor changes. At high concentrations, the most complex amyloid structures, presumably protofibrils,

are observed by ECD (Figure 3a–c), characterized by the intense aromatic interaction in the Tyr side-chains (1L_b transition), suggesting a highly ordered structure. At concentrations above ~ 1.4 mM, amyloid formation accelerates, with the appearance of a positive ECD band at ~ 235 nm, associated with Tyr side-chain π – π interactions (Figure 3a,b). In contrast, at lower concentrations (~ 1.26 mM, Figure 3a—orange curve), Tyr self-alignment is delayed, taking weeks to manifest. These findings highlight that both pH-controlled charge distribution and concentration influence amyloid formation. In addition, vibrational circular dichroism (VCD) spectroscopy, monitoring the C=O stretching mode at 1628 cm^{-1} , shows increased intensity at higher concentrations, reflecting enhanced amyloid organization and reduced internal dynamics (Figure 3d,f).^[24,25] The intensity of this band increases at higher concentrations, indicating that the amyloid structure becomes more organized along with the reduction of internal dynamics, affecting the C=O vibrational mode. The spectrum of amide I' region from 1600 to 1700 cm^{-1} was deconvoluted into two bands, one associated with the parallel β -sheet (1628 cm^{-1}) and the other with the amide band of the free Gln/Asn side-chain amides (1673 cm^{-1}). (Figure 3e)

Increasing the heptapeptide concentration up to 5 mg/mL (and above, e.g., 10 mg/mL) drastically alters the VCD spectra,

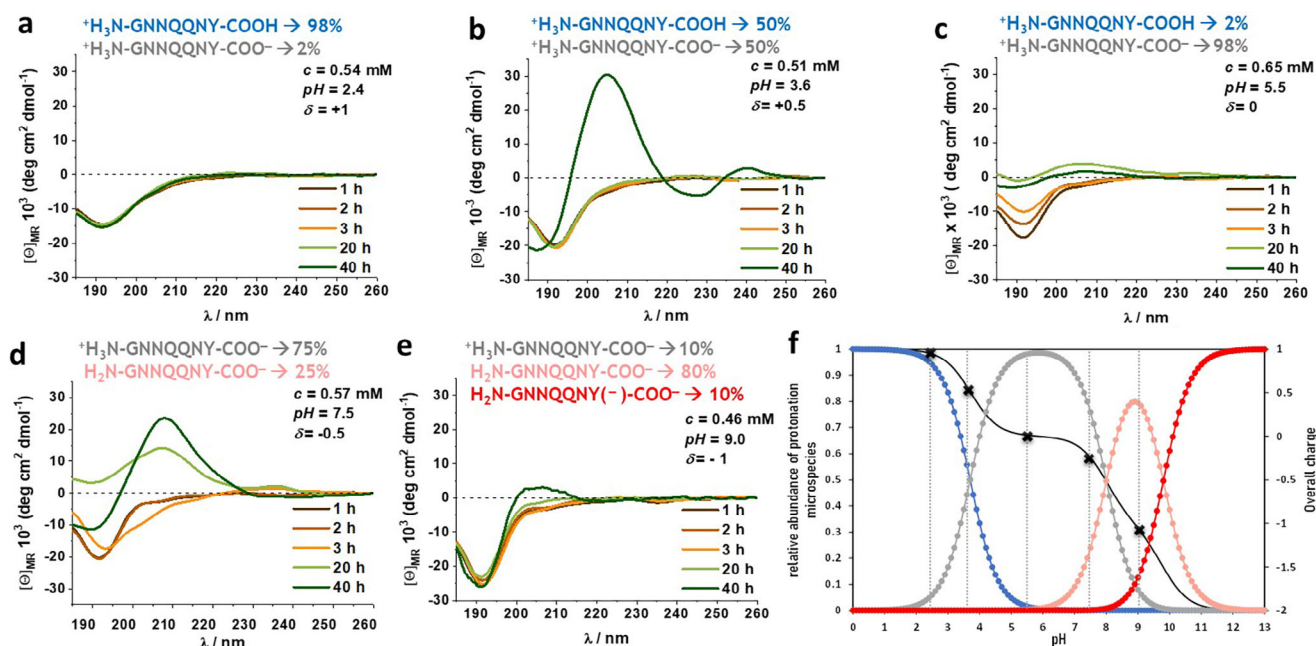


Figure 2. pH-induced ECD spectral changes of GNNQQNY in water: The time-dependent ECD spectra obtained at 37°C are arranged clockwise (a–e) and the abundances of the pH-dependent differentially charged species (f) (colors identical to the colorings of the sequences on a–e). Black x signs indicate the conditions under which the spectra were recorded: a) pH 2.4: $\delta = +1$, b) pH 3.6: $\delta = +0.5$, c) pH 5.5: $\delta = 0$, d) pH 7.5: $\delta = -0.5$ and e) pH 9.0: $\delta = -1$. The different charge states as a function of pH are represented by blue, grey, pink, and red colors. No amyloid was formed below pH 2.4 and above pH 9.0. The U-type spectrum (negative maximum at ~ 193 nm) ($t = 0$) indicates that the oligopeptide has an unstructured backbone which is gradually shifted to a B-type (negative maximum at ~ 192 nm and a positive maximum at ~ 205 nm), indicating the formation of β -strands and β -sheets.

with a very intense negative couplet at 1617 cm^{-1} and a positive peak at 1631 cm^{-1} (Figure 3f). However, the FT-IR spectrum shows only a slight shift in peak position, suggesting that the β -sheet structure persists and “solidifies” over time, growing more ordered, as indicated by ECD data. The maturation of the amyloid is also evident from the shift in the IR signal of side-chain amide groups ($1673 \rightarrow 1647\text{ cm}^{-1}$) for Asn and Gln residues. These observations suggest the buildup of a parallel β -sheet network, similar to those seen in crystal structures.

At lower concentrations (1 mg/mL), the ECD spectrum of GNNQQNY is typical of a β -sheet-assembled amyloid, while at higher concentrations (10 mg/mL), the spectrum differs due to strong chiroptical signals from Tyr side-chains (Figure 4a, dashed and solid line). The π - π interactions between aromatic side-chains act as sensors, signaling the formation of a more compact amyloid protofilament structure. This is further supported by the decomposition of the broad IR peak at 1622 cm^{-1} , where characteristic β -sheet bands (1627 cm^{-1}) and aromatic ring vibrational bands (1616 cm^{-1} and 1516 cm^{-1}) are identified. The formation of a highly ordered amyloid protofilament structure is confirmed by both vibrational and electronic chiroptical data (Figure 4b, lower panel).

2.4. Higher-Order Amyloid Structures

To investigate the role of the H-bond network, centered around the Gln side-chains, in stabilizing the amyloid structures of GNNQQNY, we engineered two mutants: Gln4Nle and Gln5Nle. The crystal structures of polymorphs (Figure 1) were utilized to

design mutation sites that would reduce, but not completely eliminate, the ability of these altered APRs to form amyloid. By following previously established optimal oligomerization conditions, we aimed to evaluate how the elimination of key side-chain interactions affects the formation of higher-order amyloid structures (Figure 1c,d). In both mutants, the absence of the carbonyl stretching sideband at $\sim 1690\text{ cm}^{-1}$ ^[26] and the preservation of the β -sheet sideband at $1627\text{ cm}^{-1} + 40\text{ cm}^{-1}$ ^[27] in FTIR spectra confirm that the parallel arrangement of amyloid-forming β -sheets remains intact in solution (Figure 4e,h).

The Gln5Nle mutation, which removes both “outer” side-chain H-bond ladders and the Gln-Tyr/Gln-Asn interactions, still allows the mutant to form β -sheets as detected by ECD spectroscopy (Figure 4g, solid line), but without any evidence of aromatic π - π interactions. FTIR data show that the β -strand orientation remains parallel, with a low-intensity band at 1515 cm^{-1} , suggesting some aromatic side-chain orientation restraint. The results indicate that the Gln5Nle mutation leads to a looser amyloid structure in solution. On the other hand, the Gln4Nle mutation, which impacts the interior of the dry-zipper interface, has the opposite effect (Figure 4d, solid line). The parallel β -sheet orientation remains preserved ($1627\text{ cm}^{-1} + 38\text{ cm}^{-1}$)^[27] but the increased hydrophobicity due to the Nle substitution within the dry-zipper increases the stability of the structure, enhancing the π - π interaction (evidenced by the ECD signal at 235 nm). In addition, the strong ECD signal at 190 nm further supports the enhanced aromatic interactions^[28] (Figure 4d). In the FTIR spectrum, the increased intensity of the amide II' band (1453 cm^{-1}), along with the vibrational band of the aromatic ring at 1614 cm^{-1} (Figure 4e, lower panel), indicates

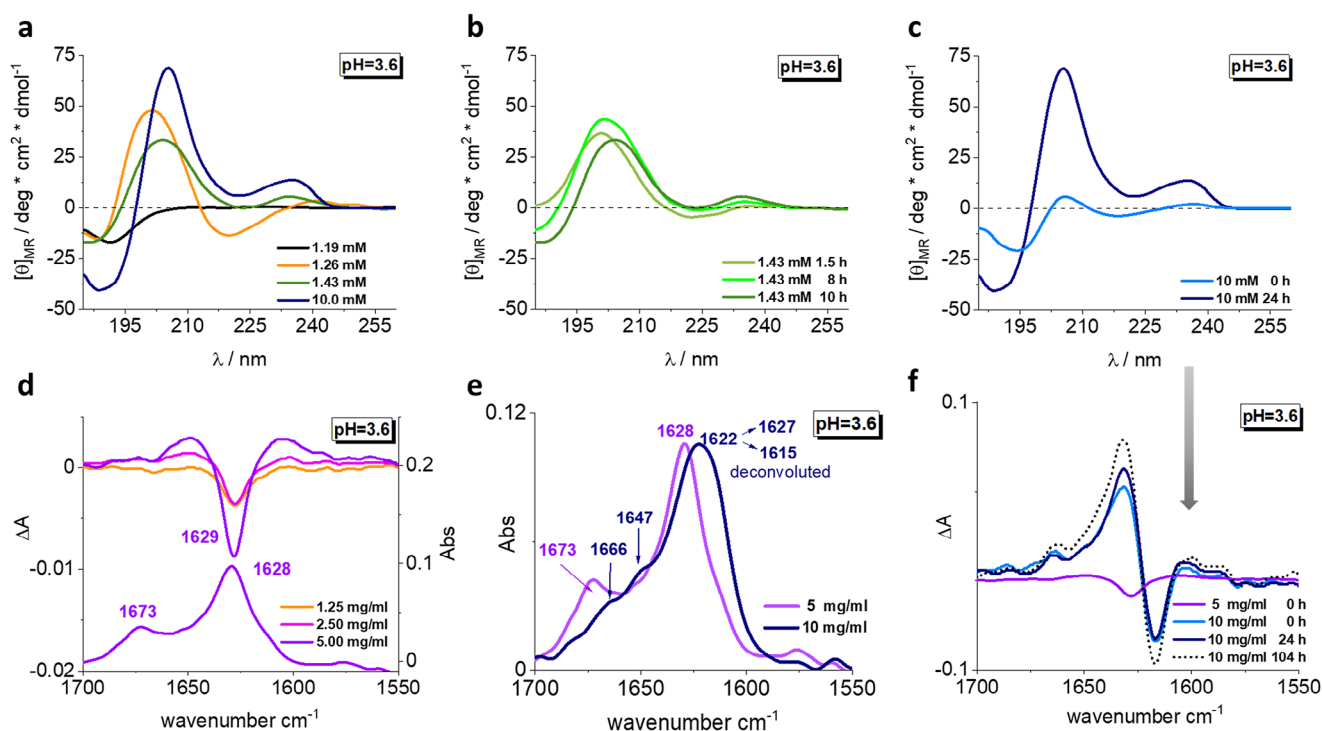


Figure 3. ECD, IR and VCD spectra of GNNQQNY peptide. Different B-type ECD spectra obtained as a function of a) heptapeptide concentration and b) the incubation time, all rising from a U-type spectrum. Over a wide range of concentrations, GNNQQNY forms amyloid: $1.26 \text{ mM} \leq c \leq 10 \text{ mM}$ ($2.8 \leq \text{pH} \leq 3.6$). Interestingly, above a critical concentration (e.g., 1.43 mM), amyloid formation and solubilization becomes steady-state as the ECD spectra change little or not at all. c) The band ($^1\text{L}_b$ transition) derived from the intense aromatic interaction further strengthens the claim that we are getting information about a highly ordered structure. d) The upper panels show the concentration dependent VCD spectra. The IR spectrum of the 5.00 mg/mL concentrated sample is shown below. The vibrational band at 1628 cm^{-1} is characteristic of the β -sheet secondary structure and the band at 1673 cm^{-1} is due to the vibration of the Asn and Gln side-chain amide groups. e) Increasing the concentration from 5.00 to 10.0 mg/mL causes a shift in the IR spectrum, with the band corresponding to the β -sheet shifting to a lower wavelength as the sheet becomes more rigid and extends. Deconvolution (see Figure S5b) reveals the side-chain vibrational bands and confirms that β -sheet retains the parallel orientation in the absence of a characteristic signal (1690 cm^{-1}) of antiparallel orientation. f) VCD spectra of the most concentrated sample as a function of time. The spectral features and the exciton couplet reveal a twisted, highly ordered structure at the protofibril level.

that the amyloid structure is even more compact than the one formed by GNNQQNY. This is consistent with the formation of a highly organized steric zipper, which decreases the hydration of the amide group and results in dominant N–H vibrations, characteristic of a twisted β -sheet.^[29,30]

2.5. Chirality Changes in Growing Protofibrils

As protofibrils grow beyond 110 nm , light scattering prevents their measurement by ECD spectroscopy, making VCD spectroscopy the preferred method. During this elongation process, oligomers align into extended β -sheets and eventually adopt a twisted conformation, rendering the carbonyl C=O stretching vibrational modes chiral. The VCD spectra of all three heptapeptides exhibit identical amide I' sidebands at 1666 cm^{-1} , confirming that their β -sheet structures consist of parallel β -strands.^[26,27,31]

For the GNNQQNY amyloid, a negative VCD couplet centered at 1624 cm^{-1} (C=O stretching mode) indicates that the protofilament, or its fundamental building blocks, adopts a left-handed twist^[32,33] (Figure 4b, upper panel). In contrast, both Nle-substituted mutants produce VCD couplets of comparable

intensity but with an opposite pattern, signifying that the filaments exhibit a right-handed twist^[34] (Figure 4e,h, upper panel). Such a sequence-dependent supramolecular chirality switch has recently been described for amyloid- β peptide APRs as well as for amphiphilic oligopeptides.^[35–38]

A particularly distinctive feature of our system is that the Gln→Nle mutation alters electrostatic interactions without significantly affecting the spatial volume or geometry of the side-chain. Nevertheless, this seemingly subtle modification is sufficient to reverse chirality, whether the mutation occurs within the dry steric-zipper core or merely influences the outer “coating” of the protofibrils.

2.6. Analysis of Amyloid Fibrils

To quantitatively compare the twisting modes and morphological variations of the higher-order amyloid structures, we extracted geometric descriptors from AFM images (Figure 5). Since the concentrated stock solutions contained densely packed mixtures of closely stacked filaments and nanocrystals, all samples were diluted to a final concentration of 0.01 mg/mL to obtain clearer AFM images (Figure S6 and S7). The

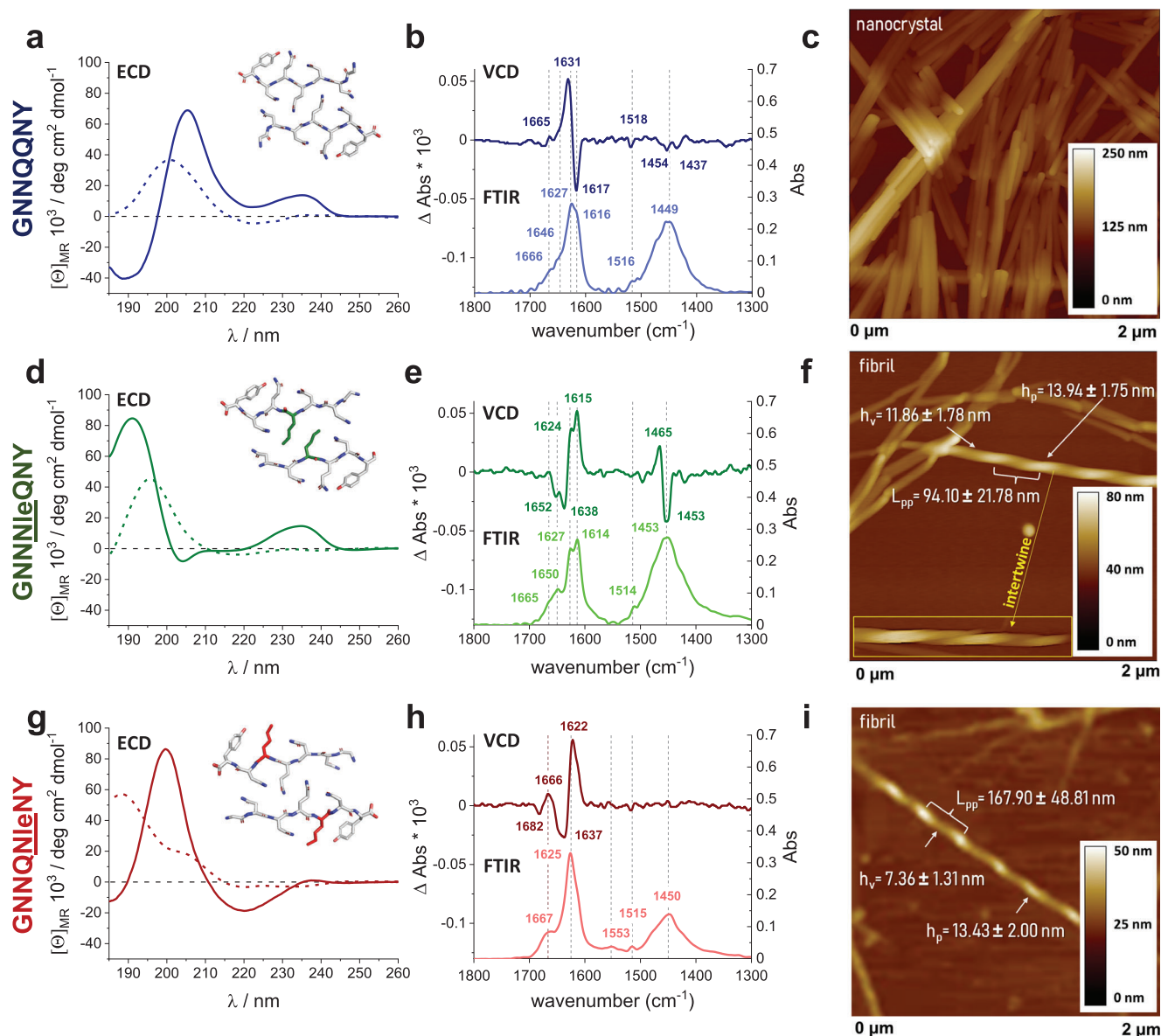


Figure 4. Comparison of the spectroscopic and macroscopic properties of the protofibrils and fibrils formed by GNNQQNY and its variants. a), d), g) ECD spectra of the peptides ($c = 1$ mg/mL (dashed line) and $c = 10$ mg/mL (solid line), pH = 3.6, temperature = 37°C ; original peptide – blue, Gln4Nle – green and Gln5Nle – red) Insert: the crystal structure of GNNQQNY with the mutation sites highlighted. a) The original sequence forms a typical β -sheet secondary structure, also in a highly ordered form, indicated by a strong band of aromatic interactions. d) The incorporation of Nle into the zipper interface makes the structure more rigid when the zip interface is tightened by increasing the hydrophobicity. The complex packing is further confirmed by the increased intensity of the aromatic interaction, not only at 235 nm, but also at 190 nm. g) Only a typical, presumably flexible β -sheet remains when the possibility of a Tyr-ring fixation is removed. b), e), h) VCD (top) and IR (bottom) spectra of the peptides. Wavenumbers in IR spectra are derived from deconvolution into Lorentz base curve sets. See Figure S5. The original sequence exhibits a left-handed twist; however, by incorporating Nle either on the inside or outside of the zipper, the twist direction is reversed, resulting in a right-handed twist. e) The chirality observed in the amide II' band in the case of the Gln4Nle variant may be a further indication of the greater complexity of the structure, suggesting a more compact folding arrangement beyond a simple pair of twisted β -sheets. c), f), i) AFM images of the formed amyloid fibrils for the three heptapeptides. In GNNQQNY, amyloid formation is very fast, so only the nanocrystalline state can be observed. In contrast, reducing the number of stabilizing hydrogen bonds may reveal structures that are likely to be trapped at lower levels of organization. In the more stable case (f), multiple filament entanglements are observed in addition to individual filaments being twisted, whereas in the looser case (i), only individual twisted filaments are observed. For further information see Figures S6 and S7. L_{pp} represents the peak-to-peak distance, h_v and h_p represent the valley and the peak height, respectively.

resulting images reveal distinct structural differences: the original GNNQQNY sequence forms a nanocrystalline structure, whereas the two Nle-substituted variants exhibit twisted filaments and fibers with opposite handedness (Figure 4c, f, i). Consistent with ECD and VCD data, the Gln4Nle variant forms a more

stable filament structure, whereas the Gln5Nle mutant results in a looser assembly. A comparison of the persistence lengths (L_{pp}) indicates that the periodicity of the amyloid fibril twisting is nearly twice as extended in the Gln5Nle variant as in the Gln4Nle variant. Despite this difference in periodicity, the fibril heights

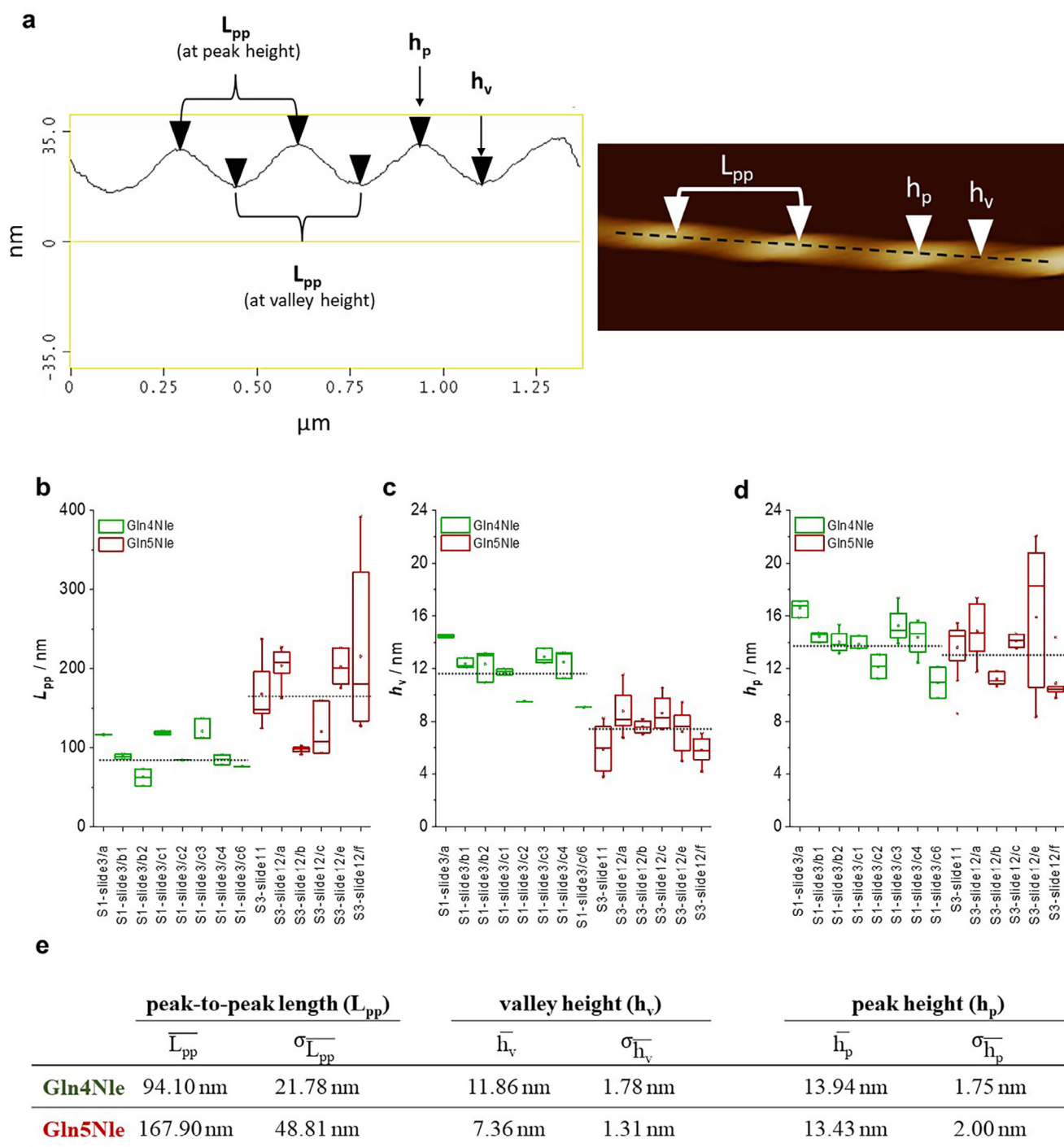


Figure 5. Morphological differences of the amyloid fibrils formed by GNNNleQNY (Gln4Nle-green) and GNNQNIeNY (Gln4Nle-red). a) Geometric descriptors of amyloid fibrils can be defined as follows: L_{pp} represents the length from peak to peak, indicating a 360° twist of the fibril. h_v (valley height) and h_p (peak height) denote the minimum and maximum heights of the twisted fibril. b–d) The box plot represents the distribution of measurement data obtained from various locations along a single fibril of each sample type. In the panels, the average values for both variants are shown as black dotted lines. e) The table summarizes the mean values and standard deviations of L_{pp} , h_v , and h_p . The specified parameters \bar{X} represent the mean of the mean of the values (L_{pp} , h_v , and h_p) recorded for each sample type (Gln4Nle and Gln5Nle) on single filaments. $\sigma_{\bar{X}}$ is the standard deviation of \bar{X} . These results show that a looser fibril has a longer twist length (L_{pp}), while a tighter, more rigid fibril has a twist length almost half as long. The maximum heights (h_p) of the fibrils are almost the same, but the minimum heights (h_v) are different.

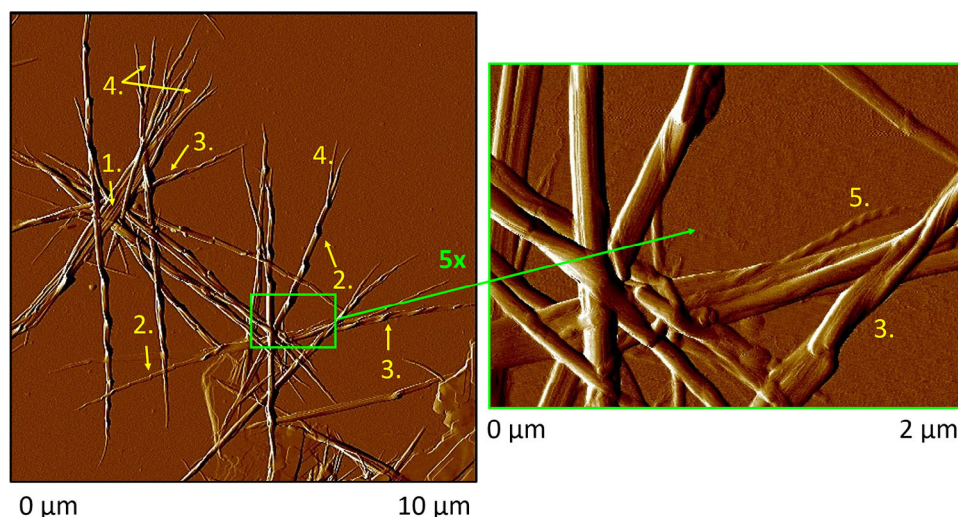


Figure 6. Different morphological states of the fibril assembly of Gln4Nle (10 mg/mL, at pH 2.0). These fibers are composed of two or more fibrils and macroscopically show a left-handed twist. This change allows us to identify different levels of organization corresponding to how the amyloids have been assembled. The numbered levels are shown in descending order of their organization: 1.) Straight fibers/nanocrystals tightly packed together; 2.) Fragmentation of thicker, partially twisted fibers along the twist; 3.) Twisting of thick fiber; 4.) Fibers break down into many thin, twisting fibrils; 5.) Twisting of thin, possibly single protofilament/filament. The amplitude image is shown for better visualization. The maximum height of the fibrils is 200 nm.

are nearly identical for both Nle variants, suggesting that their outer diameters remain comparable. However, the valley heights (h_v) differ: the more elongated Gln5Nle fibrils exhibit lower h_v , whereas the Gln4Nle fibrils display approximately 50% higher h_v , indicating a more tightly packed filament arrangement.

2.7. Supramolecular Structures of Amyloid Fibrils

For all three peptides, the protofibril-sized amyloids (lower level of organization) studied by ECD and VCD exhibit twisted nanostructures (see above). AFM imaging allows us to retrieve information on twisting at a higher level of organization.^[12] Interestingly, GNNQQNY fibrils do not display twisting; instead, the wild-type fibrils appear as densely packed, thick, and rigid β -strands, approaching a monocrystalline state (Figure 4c). In contrast, the amyloid filaments formed by the Gln4Nle variant exhibit right-handed twisting at the fiber level, as observed by AFM. This is opposite in handedness to the twist detected by VCD at the protofibril level. The presence of the amide II' band further indicates that these filaments form a more complex assembly than a simple twisted pair of β -sheets, suggesting the gradual build-up of an extensive and rigid filamentous network. Thus, while FTIR/VCD data reveal the twist of protofibrils at the lower level, AFM characterizes the architecture of fibers at a higher level of organization. This suggests that the right-handed protofilaments and filaments of Gln4Nle assemble into a meso-structure with an overall left-handed twist (Figure 4f). Such a shift in twist direction is reminiscent of right-handed α -helices forming tightly packed coiled-coil structures that adopt a left-handed supercoil at the nano-structural level.^[39]

Further insights into amyloid assembly emerge from high-resolution AFM images, highlighting intermediate structural transitions (Figure 6). A large unit consisting of multiple fibers packed together is visible (Figure 6, #1), resembling crystalline

packing. These thick, straight fibers undergo a transition into a twisted structure as they extend (Figure 6, #2, #3), before disassembling into individual filaments at their termini (Figure 6, #4). Notably, these individual filaments retain a distinct twist (Figure 6, #5). This hierarchical organization underscores the high degree of order and complexity inherent to amyloid structures.

Our findings suggest that as amyloid assembly progresses, increasing interaction surfaces and the growing number of favorable interchain interactions lead to a transition from initial right-handed protofilaments to larger fiber bundles with a left-handed superstructure. Therefore, tracking the entire assembly process—from molecular to supramolecular organization—requires complementary experimental techniques, spanning chiral spectroscopy to high-resolution imaging.

In summary, we characterized the fibril-forming sub-steps of the amyloidogenic model sequence GNNQQNY, focusing on two interaction hot-spots (Q4 and Q5) modified via isosteric, but electrostatically distinct Gln→Nle substitutions. Observations are summarized in 4 steps. 1) Protofibril characterization is as follows. Optimizing the β -sheet formation parameters (1–10 mg/mL, pH = 3.6, T = 37°C, mixing) enabled the identification of the β -fold structure and stabilizing aromatic interactions (Figure 3). FTIR and VCD spectroscopy confirmed stable β -sheet structures, evidenced by a carbonyl vibration shift from 1633 cm^{-1} to 1627 cm^{-1} .^[25] The observed vibrational sideband at 1666 cm^{-1} confirmed a parallel β -sheet arrangement^[25,27] (Figure 4b,e,h). The amide ladder, formed by Asn and Gln H-bonds, was prominently detected in the IR spectrum. Tyr side-chains formed a tyrosine-ladder, stabilized by π - π interactions, leading to increased vibrational intensity of aromatic rings. VCD spectra identified a left-handed twist,^[34] characteristic of amyloids, with GNNQQNY forming a nanocrystal without apparent high-level twisting (AFM images). 2) Impact of Gln→Nle substitutions on structure. Gln4Nle and Gln5Nle variants retained the β -sheet-forming propensity, maintaining parallel orientation but

inducing a right-handed amyloid fibril twist^[34,41] (Figure 4e,h). Structural consequences varied depending on the substitution site. i) Gln5Nle is an outward-facing position: the loss of hydrogen bonding potential increased aromatic side-chain mobility, disrupting a stabilizing interaction. This was evidenced by the disappearance of the ECD aromatic band at 235 nm (Figure 4g) and the absence of aromatic ring stretching in FTIR, indicating reduced rigidity and increased conformational flexibility. The diminished Tyr ladder interactions decreased inter- β -sheet alignment. ii) Gln4Nle is forming a steric zipper interface: the structure became more compact, with enhanced aromatic interactions. The formation of a fibrous structure was promoted by both face-to-face and face-to-edge π - π Tyr interactions. VCD analysis revealed a right-handed filament twist at the lower level, which at the macroscopic level transitioned into a left-handed fibril twist.^[41] 3) Hierarchical twisting mechanism observed. The seemingly opposite twists observed via VCD (lower level) and AFM (higher level) can be explained by hierarchical packing, analogous to right-handed α -helices forming left-handed coiled-coils.^[42] Characteristic descriptor comparisons showed similar h_p values but different h_v values for Gln4Nle and Gln5Nle, supporting the hypothesis that thicker, more rigid fibrils arise from the twisting of thinner fibrils. AFM images confirmed that fiber ends split into twisted filaments (Figure 6). 4) Crystallization and packing constraints detected. The absence of single-crystal formation for either Nle variant is attributed to hierarchical twisting, which prevents amyloid packing into a translationally symmetric arrangement. AFM images exclusively showed single, thin, flexible, yet twisted amyloid filaments for both Nle variants, contrasting the microcrystal formation observed in the wild-type sequence (Figure S7d–f).

Twisting introduced can make nanostructures more compact and thus, energetically more favorable. The amyloid formed from GNNQQNY exhibits a left-handed twist at the protofilament level, as measured by VCD. However, the energy difference between the twisted and straight structures is minimal, with the straight form being only ~ 1.18 kcal/mol per peptide ($T = 300$ K) less stable, corresponding to approximately two buried H-bonds.^[40] As these twisted protofilaments pack together, the increasing number of H-bonds formed between them induces straightening. Consequently, at the macroscopic fiber level, twisting is no longer observable, giving rise to nano-crystalline amyloids (Figure 4c). Since the origin of the twist stems from side-chain interactions, replacing Gln with Nle introduces hydrophobic interactions that promote right-handed twisted β -sheets at the protofilament level, as confirmed by VCD. However, these dispersive interactions stabilize the β -fold nanostructure in an ambiguous manner. Specifically, the right-handed twisted protofilament structure of Gln5Nle is hindered by the flexibility of the Tyr rings. In contrast, the Gln4Nle substitution enhances the hydrophobicity of the steric zipper, resulting in a more rigid protofilament structure. In both cases, replacing Gln with Nle eliminates the extensive side-chain H-bonding network present in the parent amyloid, leading to a left-handed fiber superstructure composed of right-handed protofibrils.^[42] A key question arises: does a change in conditions induce chirality inversion, as observed previously,^[32,34,41] or is it solely

the altered side-chain interactions that favor the right-handed structure over the left-handed one?^[40] Based on our current experimental data, we conclude that these effects cannot be disentangled. Another question is the size range at which this phenomenon occurs. Currently, modeling amyloid systems of this scale is computationally prohibitive, as the required *ab initio* molecular modeling remains a limiting factor. As β -folded structures increase in size, newly formed H-bonds contribute to the growing stability of protofibrils and fibrils. Larger assemblies thus exhibit increasing structural complexity. As fibrils aggregate and interact, their collective behavior may influence the direction of twist, even if only macroscopically—such as the coiled-coil-like structural adaptation observed for Gln4Nle. Alternatively, at larger sizes, the energetic proximity of opposing twist directions may become even closer. At each hierarchical level of amyloid assembly, distinct stabilizing interactions dominate, and as structural complexity increases, environmental factors influence smaller oligomers, making hydrophobic interactions more dominant and leading to polymorphic structures.^[30]

3. Conclusion

By integrating advanced spectroscopic techniques (ECD, FTIR, VCD) with high-resolution imaging (AFM), we traced the entire amyloid self-assembly pathway, from monomeric peptides to oligomers, protofibrils, fibrils, and fiber nanostructures. Using targeted amino acid substitutions in the GNNQQNY model system, we selectively disrupted hydrogen bonding to control and dissect individual stages of amyloid formation. These Gln \rightarrow Nle mutations allowed us to decelerate or even stall self-assembly at critical transition points, providing an unprecedented view of structural stabilization mechanisms that drive amyloid polymorphism. For the wild-type GNNQQNY, self-assembly is extremely rapid, masking many intermediate structures.^[43] However, by studying Nle-substituted variants, we revealed that amyloid formation follows a hierarchical process: 1) β -sheet arrays form first, 2) π - π stacking of Tyr residues initiates further oligomer growth, 3) protofibrils adopt chiral twists, and 4) higher-order fibrillar or nanocrystalline architectures emerge. While GNNQNLleNY stabilizes at the protofibril stage, GNNQQNY progresses to achiral nanocrystals, and GNNNleQNY develops into twisted chiral fibers, highlighting how subtle sequence variations dictate polymorphic outcomes. The presence or absence of inter-strand H-bonding networks governs whether amyloids stabilize as chiral fibrils or microcrystalline nanostructures. If fibril twisting remains a dominant factor, chirality is preserved even at the highest 3D-structural levels. However, if hydrogen bonding overtakes steric and π - π interactions at a critical stage, a translationally symmetric nanocrystal emerges instead of a chiral fiber. Our findings demonstrate that amyloid polymorphism is a delicate balance of hierarchical twisting, solvent interactions, and energy-minimizing packing arrangements. Understanding these molecular triggers and structural determinants is not only crucial for decoding the pathogenicity of disease-associated amyloids, but also for rationally designing functional amyloid materials

with tunable mechanical and biochemical properties. By mapping the key forces driving amyloid stability and polymorphism, our study paves the way for future applications in biotechnology, nanomedicine, and amyloid-based therapeutics.

4. Experimental Section

Peptide Synthesis and Purification: The *N*-terminal fragment of Sup35 yeast prion protein, the ⁷GNNQQNY¹³ heptapeptide and its Nle variants (Gln4Nle and Gln5Nle) were prepared by solid-phase peptide synthesis and flow chemical methods^[44,45] using the Fmoc/^tBu strategy. TentaGel preloaded resin (containing the first C-terminal amino acid) was used for the synthesis, while coupling was performed with OxymaPure and DIC reagents and DMF was used as a solvent. The reaction took place at 80°C and at a pressure of 70–90 bar. Oligopeptides were cleaved from the resin using a mixture of 2.5 v/v% triisopropylsilane, 2.5 v/v% water and 95 v/v% TFA at room temperature with stirring for 3 h. After evaporation of the TFA, the residue was precipitated in cold diethyl ether, washed three times with fresh ether and finally dried under vacuum. Crude peptides were purified by reverse phase HPLC (Jasco LC-2000Plus HPLC system) using C18 column (Phenomenex Kinetex 5 μ m 150 \times 21.2 mm,) with gradient elution under the following parameters: initial 10-min isocratic elution with 100% A eluent (water), followed by a gradient slope of 0.5 v/v % B (MeCN) per min and then collected fractions were lyophilized. Analytical purity was controlled both by MS (HR MS- Orbitrap) and analytical HPLC (see Figure S1, Table S1 and Figure S2a–f).

Sample Preparation for ECD Measurements: Peptides were dissolved in bidistilled water at the concentration range of 0.5–1.5 mg/mL. The concentration of 5-fold diluted samples were determined by NanoDrop Lite Spectrophotometer (Thermo Scientific), using molar extinction coefficient (ϵ = 1280 M⁻¹cm⁻¹) of a model compound Gly-L-Tyr-Gly at 280 nm.^[46] The pH of the peptide solution was determined by Orion Star A211 pH meter (Thermo Scientific). pH was adjusted with 0.1 M HCl and 0.1 M NaOH in the range pH 1.5–10.0. During time-dependent ECD measurements, peptide solution was stirred with a magnetic stirrer at 500–600 rpm and incubated at 37°C. The VCD and AFM samples were also measured by ECD, and sample preparation was performed as described for VCD and AFM measurements. (10 mg/mL in D₂O)

ECD Measurement: The UV-CD measurements were performed on a JASCO (Tokyo, Japan) J-810 and J-1500 spectropolarimeter fitted with a Peltier. Each spectrum was the average of five scans collected in the far UV (185–260 nm) and the near UV (230–325 nm) range with a 0.1 and 1 mm path length quartz cell, respectively. For measuring the VCD and AFM samples, 0.01 and 0.1 mm path length quartz cuvettes were used as above for the FUV and NUV ranges. The following settings were used throughout the measurements: a temperature control system at room temperature, the bandwidth of 1, 0.2 nm step size, 4 s response time and a scan rate of 50 nm/min. All spectra were obtained as the average of five scan and were corrected by subtracting the solvent spectrum acquired under identical conditions. All CD data were processed from mDeg to mean residue ellipticity (deg cm² dmol⁻¹) using the Spectra Analysis function of Jasco Spectra Manager, to account for the concentration differences.

Sample Preparation for VCD Measurements: The investigated peptide sequences (GNNQQNY, GNNNleQNY, GNNQNIleNY) were synthesized, purified, and analytically characterized in house. The

samples were dissolved in 0.01 M HCl solution and lyophilized to get rid of residual TFA. After that, the samples were repeatedly dissolved in H₂O to adjust their pH to 3.6. Finally, the samples were lyophilized two more times in D₂O to completely replace water. The samples were dissolved in 10 mg/mL immediately before the measurement.

VCD Measurement: All VCD spectra were recorded in D₂O with a Bruker PMA 37 VCD/PM-IRRAS module connected to an Equinox 55 FT-IR spectrometer at a resolution of 4 cm⁻¹. The ZnSe photoelastic modulator of the instrument was set to 1600 cm⁻¹, and an optical filter with a transmission range of 1900–1200 cm⁻¹ was used in order to increase the sensitivity in the amide I–II' spectral region. The instrument was calibrated for VCD intensity with a CdS multiple-wave plate. A CaF₂ cell of 0.055 mm path length was used, and temperature controlled by Thermo/HAAKE DC30-K20 circulating bath. In order to improve the S/N ratio, spectra were averaged for 5 h. Baseline correction was achieved by subtracting the spectrum of the solvent obtained under the same conditions. The collected interferograms were processed using OPUS 6.5 software.

FTIR Spectrum Analysis: IR spectra were calculated from the single-channel DC spectra of the sample and solvent, respectively. Spectrum were decomposed into several Lorenz curves with OPUS 6.5 built in Curve Fit evaluation method. With this decomposition, the individual vibrations of each structural feature can be identified, allowing the differences between structures to be characterized. All fitted curves give an RMSE \leq 0.01, which means the results are reliable.

Sample Preparation for AFM Measurement: The preparation of the silicon single crystal was carried out by sonication in acetone to remove dust and grease. The vacuum dried plate was used for sample application. The deuterated peptide samples were dissolved in D₂O (~4 mg/400 μ L) at a concentration of 10 mg/mL, then stirred for 24 h with 300–400 rpm at 37°C. After 24 h, the stock solution and its three dilutions (10–100–1000-fold) were dropped onto a silicon single crystal in a volume of 1 μ L and allowed to dry.

AFM Measurement: AFM scans were performed in ambient condition, at room temperature, using a Dimension 3100 AFM equipped with a NanoScope IIIa controller (Digital Instruments/Veeco, USA) in 512 \times 512 pixel resolution. Nanosensors PPP-NCHR-20 type silicon cantilevers with the following parameters, mounted at 10° with respect to the sample stage plane, were used in Tapping Mode: thickness: 40 \pm 1 μ m; length: 125 \pm 10 μ m; width: 30 \pm 7.5 μ m; typical resonance frequency ~293 kHz; force constant: 10–130 N/m; aluminum-coated top; tip height: 10–15 μ m; typical tip radius < 7 nm; tip half cone angle along the cantilever axis: 10°. To correct for tilt, a 1st order plane fit was applied to the raw image data, followed by a 0th order flattening.

Curve Resolution with Gaussians: In our attempt to decompose ECD curves, we aimed to represent them with the least number of Gaussian curves while maintaining accuracy. Initially, the curve is represented by the function $f(x) = 0$, and then we added Gaussian curves that best matched the original curve. The process ends when the original and fitted curves are sufficiently close within a certain error limit, and we avoid adding unnecessary Gaussians. Our goal was to minimize the number of curves while maximizing precision.

Acknowledgments

We would like to thank Máté Sulyok-Eiler for providing us with the Sc values from the crystal structures, Dóra K. Menyhárd for the improvement of the manuscript and Bálint Varga for the ECD curve deconvolution into Gaussian curves. This work was completed in the ELTE Thematic Excellence Program supported by the Hungarian Ministry for Innovation and Technology (**Szint-Plus**). Project no. 2018–1.2.1-NKP-2018–00005 has been implemented with the support provided from the National Research, Development, and Innovation Fund of Hungary, financed under the 2018–1.2–1-NKP funding scheme (**HunProtExc**). Project number RRF-2.3.1–21–2022–00015 is implemented with the support of the European Union's Recovery and Resilience Facility (**PharmaLab**). The scientific work publicised in this article was reached with the sponsorship of Gedeon Richter Talentum Foundation in framework of Gedeon Richter Excellence PhD Scholarship. F. Bencs was supported by the pharmaceutical company Gedeon Richter.

Conflict of Interests

The authors declare no conflicts of interest.

Data Availability Statement

The data that support the findings of this study are available in the supporting information of this article.

Keywords: β -sheet self-assembly · amyloid polymorphism · chiroptical spectroscopy · hydrophobic core stabilization · steric zipper interactions · sup35 GNNQQNY peptide

- [1] S. Lövestam, D. Li, J. L. Wagstaff, A. Kotecha, D. Kimanius, S. H. McLaughlin, A. G. Murzin, S. M. V. Freund, M. Goedert, S. H. W. Scheres, *Nature* **2024**, 625, 119.
- [2] D. Eisenberg, M. Jucker, *Cell* **2012**, 148, 1188.
- [3] G. Burra, M. B. Maina, L. C. Serpell, A. K. Thakur, *J. Mol. Biol.* **2021**, 433, 166732.
- [4] M. Haratake, T. Takiguchi, N. Masuda, S. Yoshida, T. Fuchigami, M. Nakayama, *Colloids Surf., B* **2017**, 149, 72.
- [5] A. Fernandez-Escamilla, F. Rousseau, J. Schymkowitz, L. Serrano, *Nat. Biotechnol.* **2004**, 22, 1302.
- [6] F. Chiti, C. M. Dobson, *Annu. Rev. Biochem.* **2017**, 86, 27.
- [7] U. Sengupta, A. N. Nilson, R. Kayed, *EBioMedicine* **2016**, 6, 42.
- [8] Y. Huang, R. Liu, *Int. J. Mol. Sci.* **2020**, 21, 4477.
- [9] D. S. Eisenberg, M. R. Sawaya, *Annu. Rev. Biochem.* **2017**, 86, 69.
- [10] R. Tycko, *Neuron* **2015**, 86, 632.
- [11] J. Nasica-Labouze, N. Mousseau, *PLoS Comput. Biol.* **2012**, 8, e1002782.
- [12] P. C. A. van der Wel, J. R. Lewandowski, R. G. Griffin, *J. Am. Chem. Soc.* **2007**, 129, 5117.
- [13] P. C. A. van der Wel, J. R. Lewandowski, R. G. Griffin, *Biochemistry* **2010**, 49, 9457.
- [14] J. Gsponer, U. Haberthür, A. Caflisch, *Proc. Natl. Acad. Sci. U. S. A.* **2003**, 100, 5154.
- [15] J. T. Berryman, S. E. Radford, S. A. Harris, *Biophys. J.* **2009**, 97, 1.
- [16] J. R. Lewandowski, P. C. A. van der Wel, M. Rigney, N. Grigorieff, R. G. Griffin, *J. Am. Chem. Soc.* **2011**, 133, 14686.
- [17] D. Horváth, Z. Dürvanger, D. K. Menyhárd, M. Sulyok-Eiler, F. Bencs, G. Gyulai, P. Horváth, N. Taricska, A. Perczel, *Nat. Commun.* **2023**, 14, 4621.
- [18] Z. Dürvanger, F. Bencs, D. K. Menyhárd, D. Horváth, A. Perczel, *Commun. Biol.* **2024**, 7, 968.
- [19] R. Nelson, M. R. Sawaya, M. Balbirnie, A. Ø. Madsen, C. Riekel, R. Grothe, D. Eisenberg, *Nature* **2005**, 435, 773.
- [20] M. R. Sawaya, S. Sambashivan, R. Nelson, M. I. Ivanova, S. A. Sievers, M. I. Apostol, M. J. Thompson, M. Balbirnie, J. J. W. Wiltzius, H. T. McFarlane, A. Ø. Madsen, C. Riekel, D. Eisenberg, *Nature* **2007**, 447, 453.
- [21] M. C. Lawrence, P. M. Colman, *J. Mol. Biol.* **1993**, 234, 946.
- [22] Y. Goto, M. Noji, K. Nakajima, K. Yamaguchi, *Molecules* **2022**, 27, 4588.
- [23] G. De Baets, L. Van Doorn, F. Rousseau, J. Schymkowitz, *PLoS Comput. Biol.* **2015**, 11, e1004374.
- [24] A. Barth, *Prog. Biophys. Mol. Biol.* **2000**, 74, 141.
- [25] A. Barth, *Biochim. Biophys. Acta, Bioenerg.* **2007**, 1767, 1073.
- [26] B. Martial, T. Lefèvre, M. Auger, *Biophys. Rev.* **2018**, 10, 1133.
- [27] R. Sarroukh, E. Goormaghtigh, J. Ruyschaert, V. Raussens, *Biochim. Biophys. Acta, Biomembr.* **2013**, 1828, 2328.
- [28] L. Wu, D. McElheny, T. Takekiyo, T. A. Keiderling, *Biochemistry* **2010**, 49, 4705.
- [29] F. Mallamace, C. Corsaro, D. Mallamace, S. Vasi, C. Vasi, G. Dugo, *Comput. Struct. Biotechnol. J.* **2015**, 13, 33.
- [30] T. John, A. Rampioni, D. Poger, A. E. Mark, *ACS Chem. Neurosci.* **2024**, 15, 716.
- [31] T. J. Measey, R. Schweitzer-Stenner, *J. Am. Chem. Soc.* **2011**, 133, 1066.
- [32] D. Kurouski, R. A. Lombardi, R. K. Dukor, I. K. Lednev, L. A. Nafie, *Chem. Commun.* **2010**, 46, 7154.
- [33] D. Kurouski, K. Kar, R. Wetzel, R. K. Dukor, I. K. Lednev, L. A. Nafie, *FEBS Lett.* **2013**, 587, 1638.
- [34] M. Shanmugasundaram, D. Kurouski, W. Wan, G. Stubbs, R. K. Dukor, L. A. Nafie, I. K. Lednev, *J. Phys. Chem. B* **2015**, 119, 8521.
- [35] M. Gruzziel, W. Dzwolak, P. Szymczak, *Soft Matter* **2013**, 9, 8005.
- [36] B. Martial, T. Lefèvre, T. Buffeteau, M. Auger, *ACS Nano* **2019**, 13, 3232.
- [37] S. J. Klawns, M. Lee, K. D. Riker, T. Jian, Q. Wang, Y. Gao, M. L. Daly, S. Bhonghe, W. S. Childers, T. O. Omosun, A. K. Mehta, D. G. Lynn, R. Freeman, *Nat. Commun.* **2024**, 15, 788.
- [38] R. Zheng, M. Zhao, J. S. Du, T. R. Sudarshan, Y. Zhou, A. K. Paravastu, J. J. De Yoreo, A. L. Ferguson, C. Chen, *Nat. Commun.* **2024**, 15, 3264.
- [39] A. N. Lupas, M. Gruber, *Fibrous Proteins: Coiled-Coils, Collagen and Elastomers*, Advances in Protein Chemistry, Vol. 70, p. 37, Academic Press, **2005**.
- [40] X. Periole, T. Huber, A. Bonito-Oliva, K. C. Aberg, P. C. A. van der Wel, T. P. Sakmar, S. J. Marrink, *J. Phys. Chem. B* **2018**, 122, 1081.
- [41] D. Kurouski, R. K. Dukor, X. Lu, L. A. Nafie, I. K. Lednev, *Biophys. J.* **2012**, 103, 522.
- [42] I. Usov, J. Adamcik, R. Mezzenga, *ACS Nano* **2013**, 7, 10465.
- [43] M. Balbirnie, R. Grothe, D. S. Eisenberg, *Proc. Natl. Acad. Sci. U. S. A.* **2001**, 98, 2375.
- [44] V. Farkas, K. Ferentzi, K. Horváti, A. Perczel, *Org. Process Res. Dev.* **2021**, 25, 182.
- [45] K. Ferentzi, D. Nagy-Fazekas, V. Farkas, A. Perczel, *React. Chem. Eng.* **2024**, 9, 58.
- [46] S. C. Gill, P. H. von Hippel, *Anal. Biochem.* **1989**, 182, 319.

Manuscript received: November 18, 2024

Revised manuscript received: March 12, 2025

Version of record online: April 21, 2025